Wave Velocities and Poisson Ratio in a Loose Sandy Martian Regolith Simulant Under Low Stresses: 1. Laboratory Investigation

J. Betancourt, P. Delage, B. Caicedo, P. Lognonné, B. Banerdt

Wave Velocities And Poisson Ratio In Loose Sandy Martian Regolith Simulant Under Low Stresses. Part 1: Laboratory Investigation

J. P. Castillo Betancourt[1,2], P. Delage[1], B. Caicedo[2], Ph. Lognonné[3], B. Banerdt[4]

[1] Ecole des Ponts ParisTech, lab. Navier-CERMES, CNRS, UGE, Marne la Vallée, France.

[2] Universidad de los Andes, Bogota, Colombia.

[3]Université Paris-Cité, Institut de Physique du Globe, CNRS, Paris, France.

[4] Jet Propulsion Laboratory, California Institute of Technology, Pasadena, California, USA.

Journal of Geophysical Journal: Planets 10.1029/2023JE007988

Key Points:

- Bender Element measurements of V_p and V_s carried out on a novel device on loose Fontainebleau sand samples used as a Mars regolith simulant.
- Investigation carried out within a so far unexplored low stress range, below 10 kPa and as low as 1.75 kPa.
- Poisson ratio observed to remain mostly constant at low stress, with a possible decrease in the zone below 5 kPa.

Abstract

Wave velocity measurements were performed on Fontainebleau sand samples used as Martian regolith simulant to investigate the elastic properties of the surface material at the InSight landing site on Mars (Elysium Planitia). Loose samples (density 1.4 Mg/m^3, density index 6%) were prepared by using the pluviation method, to mimic the low regolith density at the InSight landing site. A novel device derived from triaxial testing was designed to measure wave velocities at low stresses along a horizontal cylindrical specimen. Four tests were made, in which the confining stress was applied by applying vacuum between 1 and 80 kPa. Wave velocities were measured by using bender elements under stresses as low as 1.75 kPa, a very low value compared to the standard stress ranges generally considered in terrestrial geotechnics (> 10 kPa). The changes in compression and shear wave velocities obey a standard power law, with however two slightly different exponents for V_p and V_s, indicating a not perfectly elastic behavior. Data showed greater variability below 5 kPa, indicating some limitations of the bender elements technique in this range. A slight decrease in Poisson ratio was detected below 5 kPa, which certainly deserves more investigation. This investigation is useful to better analyze the data of the InSight mission, both in terms of wave propagation at surface and to interpret some in-situ elastic tests carried out with the scoop. These data are interpreted in the light of a granular contact mechanics theory in a companion paper.

Plain Language Summary

The lander of the InSight mission placed on Mars a highly sensitive seismometer to detect seismic waves from Marsquakes and meteorite impacts. To help analysing the seismic waves, a special device was developed to measure wave velocities on a loose sandy simulant mimicking the surface regolith, with wave emitting and receiving transducers placed on both sides of a cylindrical sand sample submitted to an external stress. Due to reduced gravity, stresses, that control the wave velocity (the larger the stress, the faster the waves) are very low at the surface of Mars. To impose low stresses (down to 1.75 kPa), we used a horizontal sample with a careful stress calculation along the sample axis, along which waves propagate. We determined the changes in wave velocity with stress (governed by a power law) and observed greater variability under 5 kPa, showing the limit of our transducers at low stresses. Based on the elasticity theory, we derived from waves velocities some parameter governing the sample deformations under changes of strain. We suspect

a slight decrease of the Poisson ratio (that characterises the radial elastic strain of a cylindrical sample submitted to an axial load) below 5 kPa. These data are deemed useful to better constrain the response of Mars sandy surface materials, at the InSight site and also in other areas for future missions on Mars.

1 Introduction

Recent interest into the elastic behavior at small strain of sands under low stresses has been gained through the investigation of the mechanical properties of the surface layer at the InSight landing site on Mars, submitted to reduced gravity ($g = 3.721$ m/s^2). Briefly, the NASA InSight mission is a geophysical mission landed on Mars (Elysium Planitia) in November 2018. The InSight lander installed on Mars' surface a highly sensitive seismometer, funded by CNES (Centre National d'Etudes Spatiales, the French Space Agency) aimed at investigating both the seismic activity and the meteorite impact activity on Mars. The lander also installed the so-called HP^3 thermal device funded by DLR (Deutsches Zentrum für Luft- und Raumfahrt, the German Aerospace Center) that comprised a self-driving penetrometer aimed at measuring the thermal flow emitted by Mars and at characterising the surface thermal properties (Spohn et al., 2018). The seismometer (Lognonné et al., 2019, 2020) provided valuable information about the seismic activity on Mars (e.g. Banerdt et al., 2018, Giardini et al. 2020, Hobiger et al., 2021) and about meteorite impacts (e.g. Garcia et al., 2022; Posiolova et al., 2022). Unfortunately, the self-driving penetrometer could not penetrate more than 40 cm deep, due to a lack of friction along its shaft (Spohn et al., 2022a and b). It provided however the surface thermal conductivity (0.039 ± 0.002 W m^{-1} K^{-1}), in agreement with orbital and in-situ thermal inertia estimates. Thermal data also allowed to derive a quite low surface density of 1.2 Mg/m^3 (Grott et al., 2021).

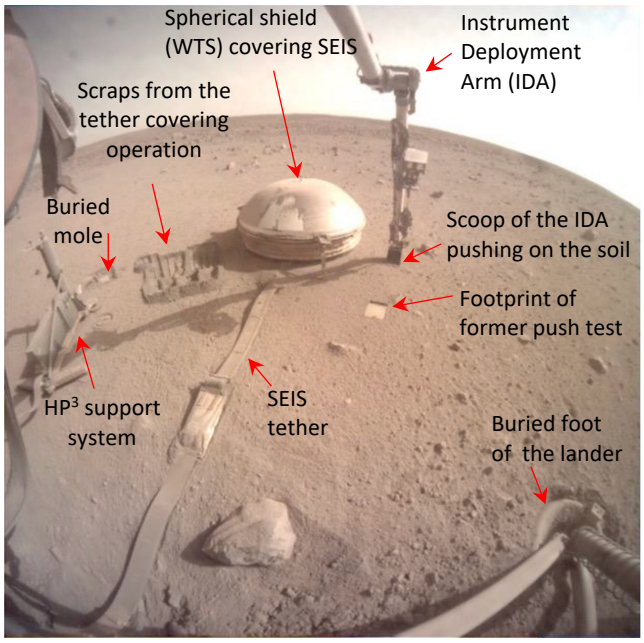

Figure 1. Image taken on Sol 1770 (i.e., the 1770th martian day of the mission) by the Instrument Context Camera of the Lander showing the hemispherical Wind and Thermal Shield (WTS, diameter 720 mm) covering the SEIS instrument, with the Instrument Deployment Arm vertically pushing on the soil at the right of the SEIS. A flat footprint made by a former push test by the IDA can also be observed. These push tests were carried out to estimate the surface elastic properties based on the sstrain derived from the SEIS response. The (black) HP^3 support system is observed on the left side, close to the place where the self-driving penetrometer has been buried. Some scraps made by the IDA scoop to cover the regolith tether for better thermal insulation can also be seen at the left of the WTS. All instruments are covered by a dust layer progressively brought by the Martian winds (Image Credit: NASA-JPL).

The InSight mission provided much information on the mechanical properties of the surface (Morgan et al., 2018, Spohn et al., 2021, Delage et al. 2022a, 2022b, 2023, Marteau et al. 2021, 2022, 2023, Verdier et al. 2023). Significant input in this regard was gained by using the Instrument Deployment Arm (IDA). The IDA, designed to place the instruments on the surface of the planet, was also used in various scrapping and piling activities carried out with the scoop at its edge (Golombek et al., 2023). Figure 1 shows a photo taken by the Instrument Context Camera of the lander on sol 1771, close to the end of the mission, illustrating these activities. The photo shows that the landing site is flat and characterised by a sandy deposit with little rock abundance, as planned from orbiter data during the landing site selection (Golombek et al., 2017). The photo also shows the hemispherical Wind and Thermal Shield (WTS) placed above the SEIS seismometer and the scraps made by the Instrument Deployment Arm (IDA) placed with its scoop in contact with the soil on the right hand side of SEIS). One also observes, left of SEIS, the scraps made by the IDA scoop during the operation of covering the SEIS tether to improve thermal insulation and

reduce glitches in the seismic signals (Golombek et al. 2023). The support system of the self penetrating thermal probe is observed on the left hand side, close to the place where the probe has been penetrated. One can observe that all devices are covered by a dust layer that finally hampered the functioning of the solar arrays, resulting in a too weak power supply to keep the instruments working. This lead to the end of the mission on 18 December 2022.

The surface layer properties are not fully understood. Due to long term wind saltation, Mars regolith particles at surface are sub-rounded to rounded (Goetz et al. 2010). Direct visual observations of the pits excavated by the rocket exhausts during landing evidenced a layer of cohesive sandy matrix containing some pebbles, called duricrust (see Warner et al. 2022, Delage et al. 2022a). It is suspected that the surface low density is made possible by inter-grains cemented bonds within a loose arrangement of regolith particles. The inter-grains cement is suspected to be due to salts deposited by thin films of water via interactions of atmospheric water vapor and soils, as suggested by chemical measurements by Viking and Mars Exploration Rover spacecraft (Banin et al. 1992, Haskin et al. 2005, Hurowitz et al. 2005).

The in-situ determination of the surface regolith elastic properties could be made by recording with the seismometer the waves emitted during the hammering sessions of the penetrometer (Brinkman et al., 2022). The mean values of compression and shear wave velocities were V_p = 119 m/s and V_s= 63 m/s, respectively, in reasonable agreement with previous lab estimations on loose sands used as regolith simulants (Delage et al., 2017).

In spite of the difference between the sandy simulants used in terrestrial lab testing (Seiferlin et al. 2008, Delage et al. 2017, Delage et al. 2022b) and the regolith at the InSight landing site, it was found interesting to further investigate the elastic properties of sandy simulants under stresses lower than those currently considered in terrestrial Soil mechanics to better analyse the properties of surface sandy regolith on Mars, that are submitted to very low stresses. To do so, a specific device was developed in the laboratory to measure wave velocities in loose sand with bender elements under low stresses. This paper presents the device and the results obtained in terms of wave velocities and Poisson ratio. In a companion paper (Caicedo et al. 2023), the data are analysed through a theory of contact mechanics accounting for the roughness of particles (Bachrach et al. 2000, Bahrami et al. 2005, Bachrach and Avseth 2008, Butt et al. 2015).

2 Wave velocity and Poisson ratio in sands

The Poisson ratio ν of sands has been determined through wave velocity measurements by various authors, including Bates (1989), Nakagawa et al. (1996), Prasad (2002), Kumar & Madhusudhan (2010) and Suwal & Kuwano (2013). The expression of ν with respect to V_p and V_s is as follows, assuming an isotropic elastic medium:

$$\nu = 0.5\,\frac{\left(\frac{V_p}{V_s}\right)^2 - 2}{\left(\frac{V_p}{V_s}\right)^2 - 1} \tag{1}$$

where V_p and V_s are the compression and shear wave velocities, respectively, given by the following expressions:

$$V_P = \sqrt{\left(K + \frac{4}{3}G\right)/\rho_b} \quad \text{and} \quad V_s = \sqrt{\frac{G}{\rho_b}} \tag{2}$$

where K and G are the bulk and shear elastic moduli, respectively, and ρ_b the bulk unit mass of the sample.

In the stress ranges considered by these authors, the Poisson ratio decreased under increased stress. Under high stresses, Prasad (2002) observed a decrease from 0.38 to 0.30 between 1 and 10.2 MPa ,with ν = 0.30 up to 20 MPa. For Toyoura sand (D_{50} = 0.19 mm, I_D = 0.68), Suwal and Kuwano (2013) showed that ν decreased from 0.175 down to 0.15 between 50 and 400 kPa. Kumar and Madhusudhan (2010) investigated the effects of stress (between 100 and 500 kPa), density index I_D between 0.4 and 0.8 ($I_D = \frac{e - e_{min}}{e_{max} - e_{min}}$, where e_{max} and e_{min} are the sand maximum and minimum void ratios, respectively) and grain size of well-sorted sands. All the Poisson ratios measured were below 0.26 and decreased with increased density index. Some data under lower stresses in a dense random pack of identical glass beads were presented by Bachrach et al. (2000), with ν ranging between 0.130 and 0.151 for stresses between 5 and 40 kPa. They also conducted in-situ wave measurements in Moss Landing beach (California, dry angular sand) using a seismic line parallel to the shoreline of 20 geophones distant of 30 cm, and a hammer (about 50 kg) applied on a metal block as source. The Poisson ratio derived from the velocity profile between 0 and 5 m (vertical stress between 0 and 78.5 kPa with a dry unit mass of 1.7 Mg/m^3) was equal to 0.15, with no increase with depth. The Poisson ratios that they determined in the lab were between 0.13 and 0.26, with a tendency to decrease i) under increased stress - more

149 significantly for fine-grained sand - and ii) under increased density index, whereas the in-situ
150 determination by Bachrach et al. (2000) evidenced a constant ν with respect to stress.
151

152 ## 3 Materials and Methods

153 ### 3.1 Fontainebleau sand as a Martian Regolith simulant

154 To account for the rounded shape of regolith grains on Mars (Goetz et al. 2010), we adopted
155 the NE34 Fontainebleau sand (see Delage et al. 2022b). It is a well-sorted silica sand (grain density
156 ρ_s = 2.651 Mg/m^3) from the Paris Basin with a median diameter D_{50} of 220 µm, (see Figure 2,
157 Benahmed 2005), to compare with the 175 µm diameter derived from thermal inertia
158 measurements in the InSight landing site (Golombek et al. 2017). The uniformity coefficient C_u is
159 equal to 1.65. The grain size distribution is presented in Figure 2a, together with a scanning
160 electron microscope photo (b) that shows that grains are sub-rounded to rounded. The minimum
161 and maximum void ratios are e_{min} = 0.54 and e_{max} = 0.86, respectively (Andria-Ntoanina 2011).
162

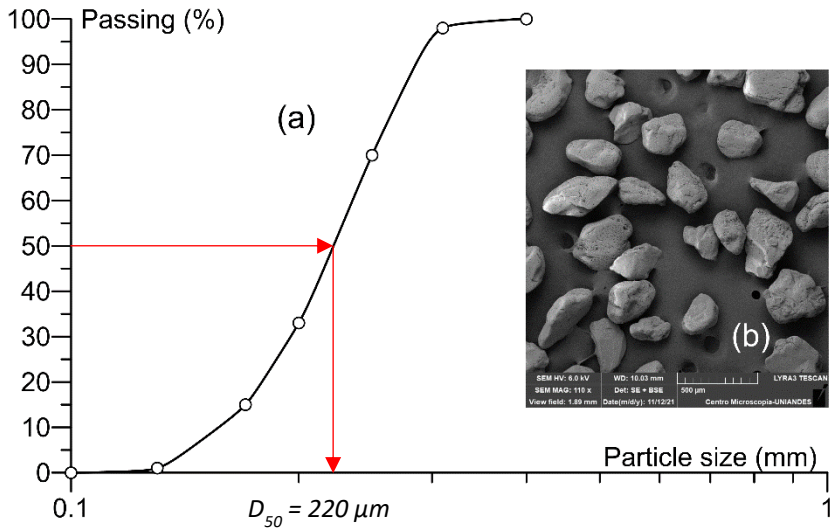

163
164
165 Figure 2. NE34 Fontainebleau Sand: (a) grain size distribution curve, and (b) SEM image.

166 ### 3.2 Sample preparation

167 The sample was prepared, as for standard triaxial testing, by using a 170 mm high mould
168 of internal diameter 100 mm into which a neoprene membrane, fixed to the base of the triaxial cell
169 and the external face of the mould at the top by using two O-rings, was maintained by applying

vacuum (80 kPa). The pluviation technique (Kolbuszewski, 1948; Cresswell et al., 1999, Benahmed, 2001, Hariprasad et al. 2016) was used to prepare a low density sample, adopting an almost null fall height (resulting in an upward speed of the sieve of 3 cm/s) and a small sand flow.

The final dimensions of the sample are 100 mm in diameter and 150 mm in height, with a density around 1.4 Mg/m^3 (void ratio $e = 0.84 - 0.82$, density index I_d = 6 - 10%). After pluviation, the sand in excess was carefully removed, the top cap was carefully placed on the flattened sand surface and the membrane was wrapped around it and fixed by an O-ring. Before dismounting the mould, the vacuum was decreased to 10 kPa, a pressure that appeared to be high enough to maintain the cylindrical shape of the sample.

3.3 Experimental setup at low stress

The wave velocity measurements were carried out by using 3 mm height bender elements (GDS brand, able to send and receive both compression P and shear S waves) inserted into the top and bottom ends of the sample. They were controlled via a signal generator producing sinusoidal waves at a fixed frequency of 10 kHz and 14 V amplitude. An amplifier was used to increase the magnitude of the received signal. Data acquisition was made through an oscilloscope, using two channels spatially located the furthest from each other, thus reducing as much as possible the crosstalk effect between bender elements (Lee & Santamarina, 2005).

In a vertical position, with a density of 1.4 Mg/m^3, the vertical stress σ_v at the base is around 2.21 kPa (the weight of the soil column). Given the low-stress range considered (below 10 kPa), the stress difference between the top and bottom of the sample was not acceptable. It was then decided to place the sample in a horizontal position (Figure 3).

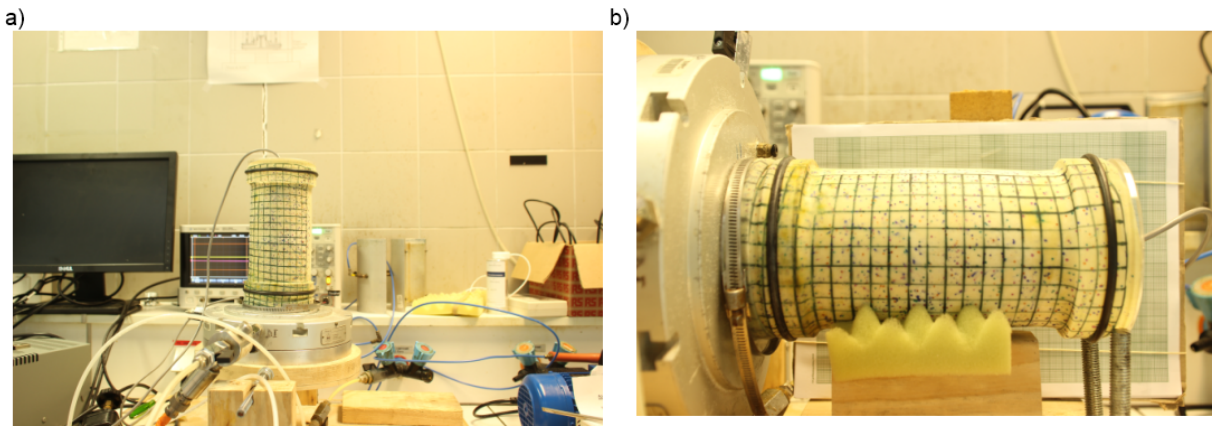

193 Figure 3. a) Sample preparation (vertical); b) Sample tested (horizontal).

194 The wave travel path along the axis of the horizontal cylindrical sample is submitted a total
195 stress σ equal to the sum of three components:

196 $$\sigma = \sigma_{vac} + \sigma_m + \sigma_{gh} \quad (3)$$

197 where σ_{gh} is the gravity-induced stress within the horizontal sample, σ_m the membrane isotropic
198 confining stress and σ_{vac} the vacuum-induced isotropic stress.

199 The stress produced by the membrane was evaluated using the solution for a small wall
200 cylinder under pressure as follows:

201 - The stiffness of the membrane was measured by imposing different forces on a membrane,
202 as shown in Figure 4a. From the linear response obtained (Figure 4b), one can derive the
203 spring coefficient k of the membrane as the ratio between the half of the applied unit load
204 and the axial strain of the membrane. The data of the Figure provide k = 1613.85 N/m.
205 - The force F_m applied by the membrane around the sample (Figure 4c) is given by $F_m = k$
206 $\Delta r/r$, where k is the membrane spring coefficient, Δr the increase in the radius of the
207 membrane between the free state and the stressed state around the sample and r the sample
208 radius. Δr was obtained by subtracting the sample perimeter from the length of the extended
209 membrane, L_m, divided by 2π ($\Delta r = r - L_m/2\pi$).
210 - Using the solution for a small wall cylinder under pressure, as shown in Figure 4c, the
211 radial stress σ_m applied by the membrane per unit length on the sample is $\sigma_m = F/r$.

212 With k = 1613.85 N/m, Δr = 2.5 mm and r = 50 mm, the confining stress due to the
213 membrane is σ_m = 1.6 kPa, a result similar to that obtained by Henkel & Gilbert (1952) and
214 Newland & Allely (1959).
215

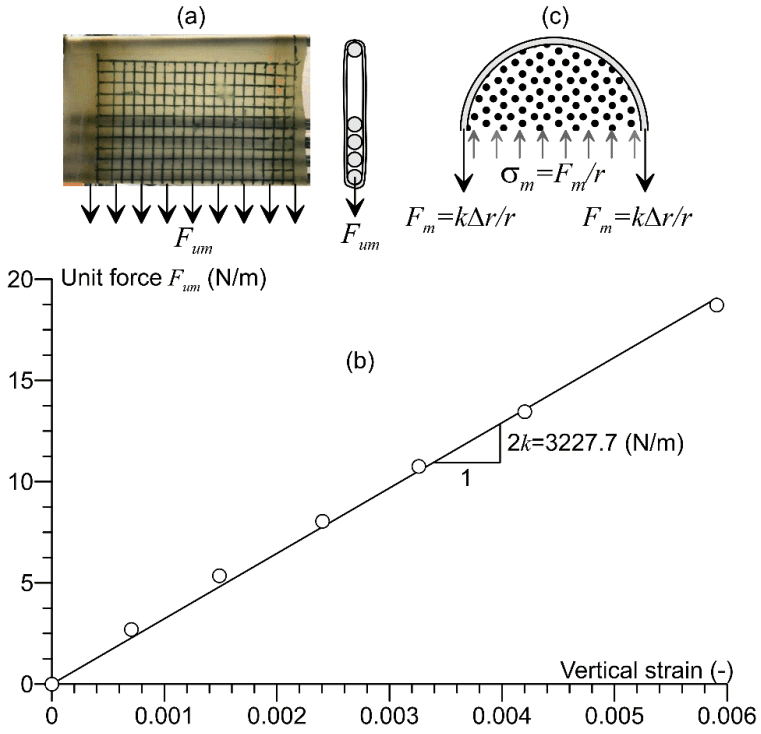

Figure 4. (a) Setup used for measuring the membrane stiffness; (b) Force/vertical strain elongation curve of the membrane; (c) Schematic drawing for computing the stress on a cylinder.

The gravity-induced stress was computed in elastic conditions by using the Plaxis 3D finite element code (see Figure 5), applying the membrane stress as a boundary condition, providing σ_{gh} = 0.75 kPa at a density of 1.4 Mg/m^3.

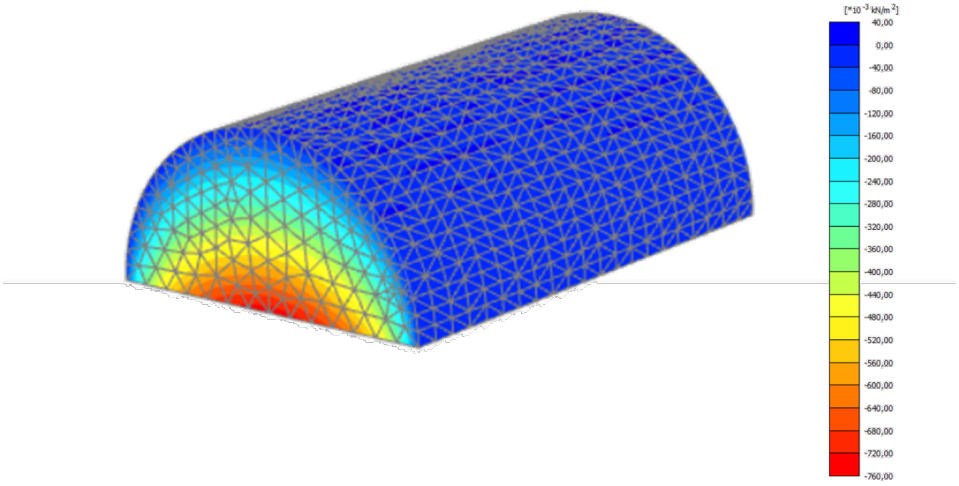

Figure 5. FEM (Plaxis 3D) elastic analyses of the sample self-weight to estimate the horizontal stress σ_{gh} on the sample axis.

The constant stress due to both gravity and the membrane is $\sigma_m + \sigma_{gh} = 0.75$ kPa. The total stress applied to the sample was changed by changing the vacuum applied within the sample. Once the (vertical) sample pluviated and the membrane fixed around it, a 10 kPa vacuum was applied before removing the mould and rotating the sample in the horizontal position, with no change observed in its size. The total horizontal stress applied on the sample axis was obtained by adding 0.75 kPa to the applied vacuum. Then, the loading path was applied by changing vacuum as follows:

- A step unloading path from 10 kPa to 1 kPa, (10 - 9 - 8 - 7 - 6 - 5 - 4 - 3 - 2 - 1 kPa) followed by reloading back to 10 kPa.
- A step loading path from 10 kPa up to 80 kPa, (10 - 20 - 30 - 40 - 50 - 60 - 70 - 80 kPa). Moreover, some tests were performed at 5 and 15 kPa to investigate eventual hysteresis effects.

Various wave measurements were carried out at each stress to assess variability and repeatability. Five waves were recorded for stresses below 10 kPa, as a higher variability was observed in this stress range. In contrast, three measurements were deemed sufficient at 15 kPa and above (the number of repetitions was chosen after interpreting the results of the initial tests).

3 Experimental results

The tests were carried out on 4 pluviated samples (EP 1 to 4), with the following measured densities: EP1=1.443 Mg/m^3, EP2=1.443 Mg/m^3, EP3=1.447 Mg/m^3 and EP4=1.452 Mg/m^3.

Determining the accurate travel time of the waves is crucial in bender element tests, and various methods have been used in the literature. They include the first inversion of the output signal and the first zero value immediately after the signal inversion (Shirley & Hampton, 1978; Dyvik & Madshus, 1985; Jamiolkowski et al., 1995; Jovičić et al., 1996; Jovičić & Vilhar, 2009), the peak-to-peak-method (Viggiani & Atkinson, 1995a), the cross-correlation frequency-domain method (Viggiani & Atkinson, 1995b; Arulnathan et al., 1998; Boulanger et al., 1998; Mohsin & Airey, 2003; Murillo et al., 2009; Murillo et al., 2011) and some methods simultaneously analysing the travel time of both P and S waves (Lee & Santamarina, 2005; Wang et al., 2017).

As seen in Figure 6, which presents the data for 70.75 kPa, an accurate determination of the travel time could be made by considering, for both P and S waves, the starting point of the sinusoidal emitted signal and that of the received P and S signals. Interestingly, there is a clear

coupling between the reception of both waves. The S wave arrival could be detected in the received P wave signal (at 0.57 ms), as commented by Wang et al. (2017). Note also that some slight oscillations due to the P wave arrival (after 0.4 ms) are detected in the S wave signal, whereas a clear increase in amplitude in the P wave signal is observed when the S wave arrives after 0.57 ms.

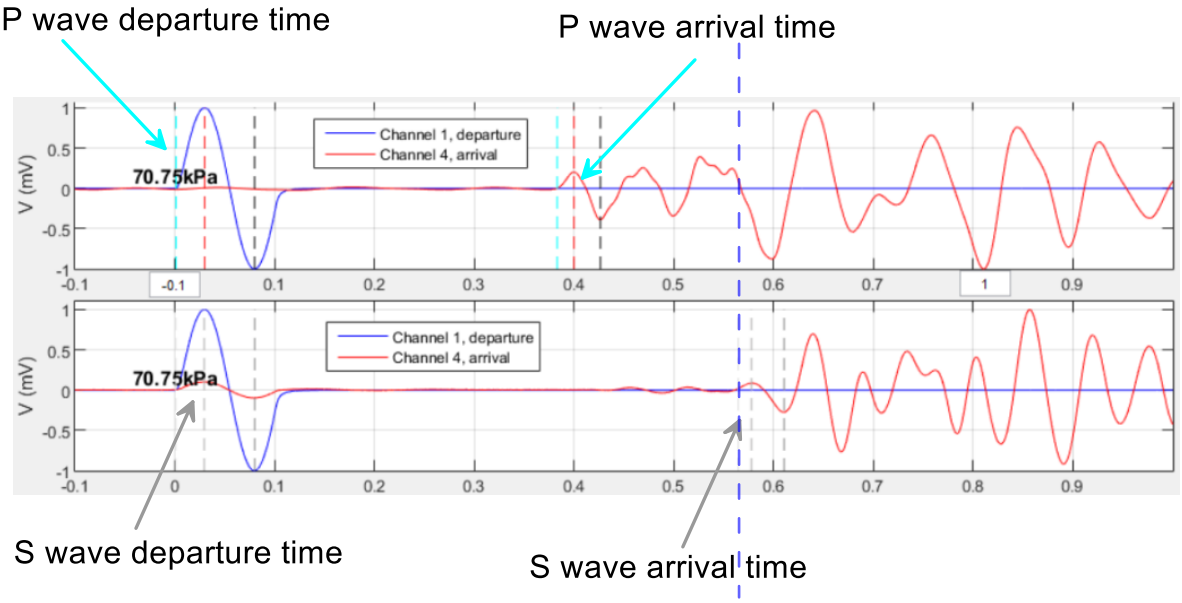

Figure 6. P and S waves under 70.75 kPa, with good correspondence between both: the S wave arrival can also be detected in the P wave signal; the arrival of the P wave creates some slight perturbations in the S wave signal (time is in milliseconds).

As seen in Figure 7, that presents both P (pink) and S (grey) signals under lower stresses (< 10 kPa), the signals become less clear at small stresses, particularly below 2.75 kPa. Besides carefully examining both signals and their coupling, the arrival time was also determined by extrapolating the trend resulting from larger stresses. The data show that bender elements can be used in (loose) sands, even under low stresses, smaller than those currently investigated in terrestrial geotechnical engineering.

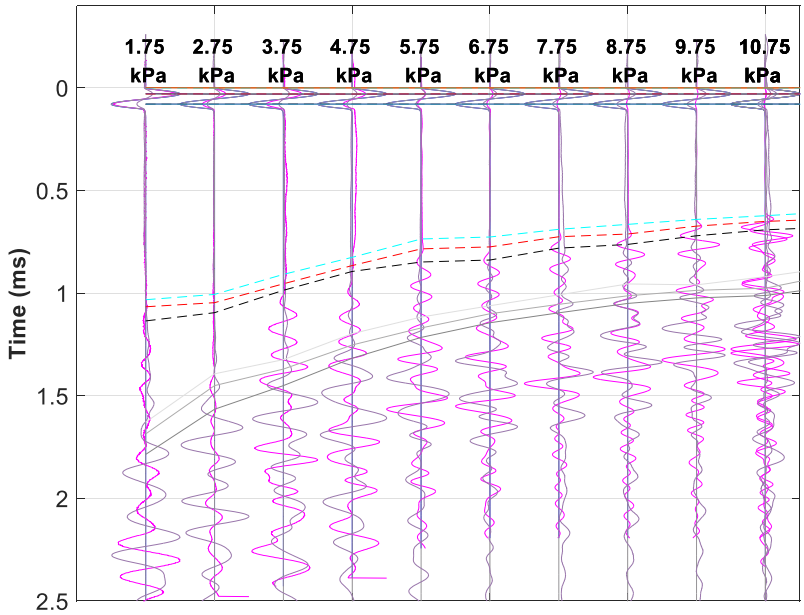

Figure 7. P (pink) and S (grey) waves detected under smaller stresses below 10 kPa.

Good agreement was also found with peak-to-peak data (calculating velocity with the tip-tip distance between bender elements, Lee & Santamarina 2005). A software (Appendix A) was implemented to interpret arrival times, visualise all P/S waves of each experimental program in a group and suggest the departing and arriving points.

Figure 8 shows the change in wave velocities with stress in the tests on samples EP1 to EP4. The shape of the curves is comparable to other data on sands (e.g. Bachrach et al. 2000, Zimmer et al. 2002, Delage et al. 2017). As indicated in the Figure, the stress path followed first decreases from 10.75 kPa to 0.75 kPa, before increasing to 10.75 kPa up to 80.75 kPa.

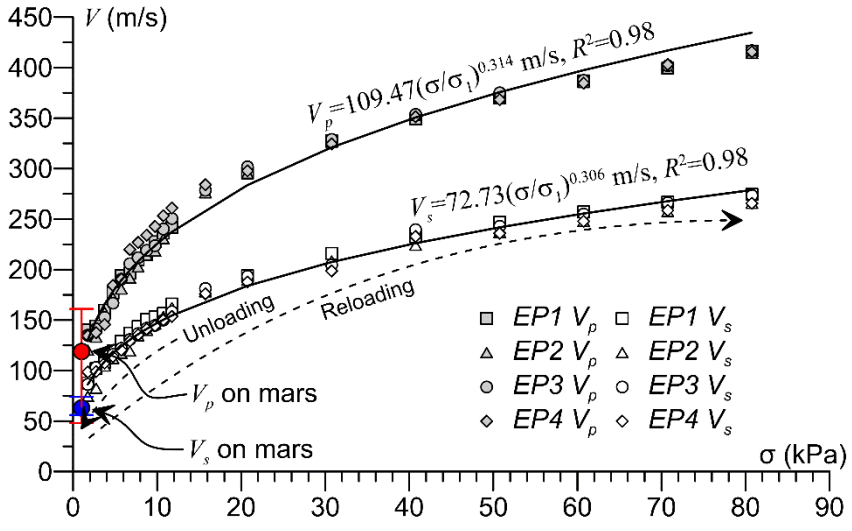

Figure 8. Measured wave velocities obtained using bender elements compared with those measured by Brinkman et al. (2022) on Mars (red and blue points).

Inspection of data along the unloading-reloading path indicates no significant hysteresis effect in both V_p and V_s curves, showing satisfactory reversibility in the response, in conjunction with slight changes in the grain assembly. Also, the variability of the measured wave velocities between the different samples is low, demonstrating good repeatability and providing confidence in the results.

As expected, the velocities decrease with decreased applied stress, according to the following equations:

$$V_{\mathrm{p}} = 109.47 \left(\frac{\sigma}{\sigma_1}\right)^{0.314} \qquad R^2=0.98 \tag{4}$$

$$V_s = 72.73 \left(\frac{\sigma}{\sigma_1}\right)^{0.306} \qquad R^2=0.98 \tag{5}$$

where σ_1 =1 kPa is a reference stress.

4 Discussion

The exponents derived from Figure 8 (Eqs 4 and 5) are slightly different for V_p and V_s, showing that our experimental data are not fully in agreement with the elasticity theory. When trying to fit V_p and V_s with the same exponent, one gets a value of 0.31, with no dependency of the Poisson ratio with respect to the confining stress. This leads however to a Poisson ratio of 0.105, in disagreement with our experimental results. The exponents values derived from Figure 13 are higher than those measured (0.22) at higher stresses between 25 and 450 kPa by Delage et al. (2017) on three other Martian simulants (Mojave Mars simulant, MSS-D and Eifel sand).

Interestingly, these data agree reasonably well with the in-situ measurements performed on Mars during the hammering campaign of the HP^3 self-penetrating dynamic probe (see Figure 1), during which emitted waves were detected by SEIS. The $V_{\mathrm{p}}/V_{\mathrm{s}}$ values determined by Brinkman et al. (2022) are reported in the figure, considering that they correspond to a vertical stress of 0.9 kPa, resulting from an average depth of 0.2 m at a density of 1.2 Mg/m^3 (Grott et al. 2022) under a gravity of 3.721 m/s^2.

Figure 9, that presents the Poisson ratios computed using Eq. 1 from V_{p} - V_{s} measurements at each point, exhibits more variability below 5 kPa. This is probably related to the difficulty of

properly measuring travel times at low stresses (see Figure 12), in a stress range for which the use of bender elements becomes more tricky.

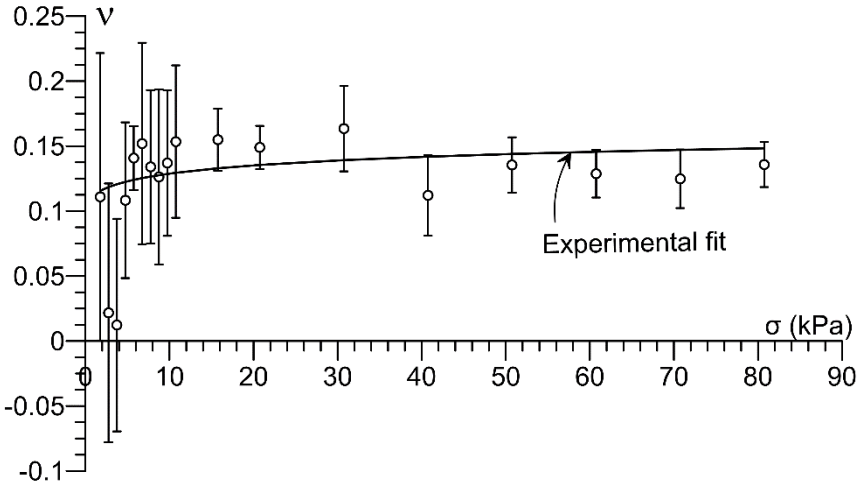

Figure 9. Changes in Poisson ratio with respect to confining stress determined from bender element measurements (points) and from the fitted curves of Figure 8 (curve).

Since the values of the exponents of Eqs 4 and 5 are close, the relationship V_p/V_s is slightly dependent on stress, with $V_p/V_s = (\sigma/\sigma_1)^{0.008}$. Therefore, from Eq. 1, the fitting equation for the Poisson ratio becomes:

$$\nu = 0.5\,\frac{2.265\left(\frac{\sigma}{\sigma_1}\right)^{0.016}-2}{2.265\left(\frac{\sigma}{\sigma_1}\right)^{0.016}-1} \qquad (6)$$

This low dependency of the Poisson ratio with respect to stress is illustrated in the curve of Figure 9 that indicates a slight decreasing trend below 10kPa, derived from both individual points and fitted curves.

The larger dispersion of our experimental data below 5 kPa indicates that bender elements are less efficient in this area. Inspection of the data of Figure 9 also shows that the changes in V_p/V_s with stress seems to somewhat differ below 10 kPa, with a less regular curvature of the data. The changes in Poisson ratio below 5 kPa would certainly deserve more investigation, in an area where the efficiency of bender elements is perhaps limited.

The velocities may be used to calculate the elastic shear modulus G (from Eq. 2) and the Young modulus $E = 2G(1+\nu)$. The results, presented in Figure 10, show how the moduli

335 decrease with decreased stress. Interestingly, the data at low stress are not far from the measured
336 value of E from interaction tests carried out with the SEIS foot on Fontainebleau sand (20 MPa at
337 3.5 kPa, Delage et. al 2022b).
338

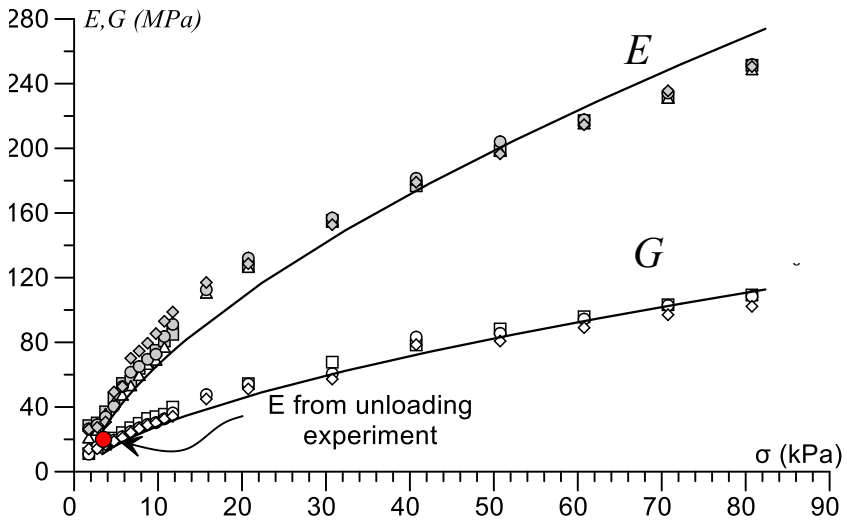

339
340 Figure 10. Changes in shear and Young modulus with respect to confining stress determined from
341 model predictions. The results from an interaction with the SEIS foot (red point) is in good
342 agreement (Delage et al. 2022b).

343 **5 Conclusions**

344 Wave measurements were performed under low stresses by using bender elements on loose
345 samples of Fontainebleau sand used as a Martian regolith simulant. This was made to better
346 constrain the elastic properties of the regolith at the surface of the InSight landing site and to help
347 interpreting in-situ elastic data obtained at surface through wave measurements (Brinkman et al.
348 2022) of indentation experiment carried out with the IDA (Delage et al. 2023). Current knowledge
349 on wave transfer in sands was extended to low stresses (< 10 kPa) by using a horizontal cylindrical
350 sample submitted to changes in vacuum (between 2 and 80 kPa). Additional stresses due to gravity
351 and to the confining membrane were carefully calibrated and accounted for. Uncertainty in wave
352 velocity determination was reduced by performing 3 to 5 measurements at each stress, and tests
353 were carried out on 4 different samples. Bender elements were able to provide wave velocity
354 measurements at stresses as low as 1.75 kPa, with however greater variability below 5 kPa. The
355 change in V_p and V_s with respect to stress followed a power law, with however two slightly
356 different exponent values, indicating that elastic hypotheses were not fully respected within the

sand sample. The calculation of the Poisson ratio ν from wave velocities measurements confirmed that ν was reasonably constant above 10 kPa. Conclusions are less clear below 5 kPa, where the bender elements measurements are less accurate. The possibility of having a decreasing Poisson ratio in this area seems still worth of investigation, to be conducted through other experimental techniques.

This study enlarged the knowledge of the elastic behaviour of sands under low-stress and low strain, a novel topic in wave velocities investigations, that was useful to interpret local wave velocity measurements carried out at the InSight landing site (Brinkman et al. 2022). Further information was also gained about the Poisson ratio under low stress, another important parameter to estimate the surface elastic response of the surface.

However, the comparison of our laboratory data on a Martian simulant with what could be the response of a true Martian regolith is not straightforward. First, one have to consider possible differences in the grain package, that is known to have significant effects on seismic wave travel. It is very probable that the packing resulting from our pluviation method on a vertical sample, that has been put horizontally afterwards, differs from the packing of surface regolith grains on Mars, that results from very long term wind saltation (through many repetitive small lateral jumps of sand grains along the wind direction). It could be that the post convenient way to mimic the resulting packing would be by trying to reproduce the saltation process on a (subrounded) sand field submitted to constant wind. Then, the best would probably to run in situ wave determination by using a line of geophones aimed at detecting an impact made on the ground, as done by Bachrach et al. 2000 on a beach in California.

Note also that direct observations and measurements made on the InSight landing site showed that the soil profile was not only made up of a sandy material. The true profile is composed of a surface 1 cm thick sand/dust layer, overlaying an around 20 cm thick loose duricrust made up of a cohesive matrix containing some pebbles, located above a 12 cm layer of sand overlaying a gravel/sand deposit (Golombek et a. 2020, Warner et al. 2022, Delage et al. 2022, Spohn et al. 2022). However, in-situ wave velocity measurements carried out during the hammering session of the HP^3 self-penetrating gauge (Brinkman et al. 2022) provided values of velocity and Poisson ratio close to those found in this work. Also, our investigation may be useful, as a first step, for other areas of Mars, where thicker deposits of sand, with dunes and ripples, have been observed (e.g., Ehlmann et al. 2017). This can also be the case for future Mars missions.

Some of the questions raised in this experimental investigation are further considered in a companion paper (Caicedo et al. 2023) in which data at small stress are analysed through a contact mechanics theory derived from Bachrach et al. (2000).

Acknowledgments

These results are part of the PhD thesis of Juan-Pablo Castillo Betancourt, financially supported by Universidad de los Andes (Colombia) and École des Ponts ParisTech (France). The authors are also grateful to NASA, CNES, their partner agencies and Institutions (UKSA, SSO, DLR, JPL, IPGP-CNRS, ETHZ, IC, MPS-MPG). The authors want to thank the contributions made by the Ecole des Ponts ParisTech Navier-CERMES technical team for setting up the experimental device, especially Loic Lesueur, Marine Lemaire, Emmanuel De Laure, Baptiste Chabot and Xavier Boulay. This paper is Insight contribution N° ICN 327.

References

Andria-Ntoanina, I. (2011). Caractérisation dynamique de sables de référence en laboratoire - Application à la réponse sismique de massifs sableux en centrifugeuse. PhD thesis, Ecole des Ponts ParisTech (in French).

Arulnathan, R., Boulanger, R. W. and Riemer, M. F. (1998). Analysis of Bender Element Tests. In Geotechnical Testing Journal, GTJODJ, 21(2).

Bachrach, R., Dvorkin, J. and Nur, A. M. (2000). Seismic velocities and Poisson's ratio of shallow unconsolidated sands. Geophysics, 65(2), 559–564. https://doi.org/10.1190/1.1444751.

Bachrach, R., and Avseth, P. (2008). Rock physics modeling of unconsolidated sands: Accounting for nonuniform contacts and heterogeneous stress fields in the effective media approximation with applications to hydrocarbon exploration. Geophysics, 73(6). https://doi.org/10.1190/1.2985821

Bahrami, M., Yovanovich, M. M. and Culham, J. R. (2005). A compact model for spherical rough contacts. J. Tribol. Oct 2005, 127(4): 884-889, https://doi.org/10.1115/1.2000982

Banin, A. et al. 1992. in MARS (eds Kieffer, H. H., Jakosky, B. M., Snyder,C. W. & Matthews, M. S.) 594–625 (University of Arizona Press, Tucson, 1992).

Banerdt, W. B., Smrekar, S. E., Banfield, D., Giardini, D., Golombek, M., Johnson et al. (2018). Initial results from the InSight mission on Mars. Nature Geosciences (13) 183 – 189.

Bates, C. R. (1989). Dynamic soil property measurements during triaxial testing. Géotechnique, 39(4), 721-726.

Benahmed, N. (2001). Comportement mécanique d'un sable sous cisaillement monotone et cyclique : application aux phénomènes de liquéfaction et de mobilité cyclique. PhD thesis, Ecole des Ponts ParisTech (in French).

Boulanger, RW, Arulnathan, R., Harder, LF, Torres, R., and Driller, M. (1998): Dynamic Properties of Sherman Island Peat, Journal of Geotechnical and Geoenviromental Engineering, ASCE, 124, (1), 12-23.

Brinkman, N., Schmelzbach, C., Sollberger, D., Pierick, J. T., Edme, P., Haag, T. et al. (2022). In situ regolith seismic velocity measurement at the InSight landing site on Mars. Journal of Geophysical Research: Planets, 127(10), e2022JE007229.

Butt, S. U., Antoine, J. F. and Martin, P. (2015). Simplified stiffness model for spherical rough contacts. Tribology-Materials, Surfaces & Interfaces 9(2), 63-70.

Caicedo B., Castillo Betancourt J. P., Delage P., Lognonné Ph., Banerdt W.B. (2023). Waves velocities and Poisson ratio in a loose sandy martian regolith simulant under low stresses. Part 2: theoretical analysis

Castillo-Betancourt Juan Pablo. (2023). juan9715/MRA-Bender-Element-data: Bender data public repository release (Release) [Data set]. Zenodo. https://doi.org/10.5281/zenodo.8161970

Cresswell, A., Barton, M. E. and Brown, R. (1999). Determining the maximum density of sands by pluviation. Geotechnical Testing Journal, 22(4), 324–328. https://doi.org/10.1520/gtj11245j

Delage, P., Karakostas, F., Dhemaied, A., Belmokhtar, M., Lognonné, P., Golombek, M. et al. (2017). An Investigation of the Mechanical Properties of Some Martian Regolith Simulants with Respect to the Surface Properties at the InSight Mission Landing Site. Space Science Reviews, 211(1–4), 191–213. https://doi.org/10.1007/s11214-017-0339-7

Delage, P., Marteau, E., Vrettos, C., Golombek, M., Ansan, V., Banerdt, W. B. et al. (2022a). The mechanical properties of the Martian soil at the InSight landing site. In Proceeedings 20th International Conference on Soil Mechanics and Geotechnical Engineering, Sydney. https://hal.science/hal-03706564.

Delage, P., Castillo-Betancourt, J. P., Caicedo Hormaza, B., Karakostas, F., De Laure, E., Lognonné, P.et al. (2022b). The interaction between the SEIS seismometer of the InSight Martian mission and a regolith simulant. Géotechnique, 1-12.

Delage P., B. Caicedo, M. P. Golombek, T. Spohn, C. Schmelzbach, N. Brinkman, et al. (2023). Investigating the Martian soil at the InSight landing site. Keynote Lecture, International Symposium IS Porto 2023, submitted to Soils and Rocks.

Dyvik, R. and Madshus, C. (1985): Laboratory measurement of Gmax using bender elements, Proc. ASCE Annual Convention, Advances in the art of testing soils under cyclic conditions, Detroit, 186-196.

452 Ehlmann B.L. et al. 2017. Chemistry, mineralogy, and grain properties at Namib and High dunes, Bagnold
453 dune field, Gale crater, Mars: a synthesis of Curiosity rover observations. Journal of Geophysical
454 Research, Planets 122: 2510–2543. https://doi.org/10.1002/2017JE005267
455 Garcia, R. F., Daubar, I. J., Beucler, É., Posiolova, L. V., Collins, G. S., Lognonné, P. et al. (2022). Newly
456 formed craters on Mars located using seismic and acoustic wave data from InSight. Nature Geoscience,
457 15(10), 774-780.
458 Giardini D., Lognonné P., Banerdt W.P., Pike W.T., Christensen U., Ceylan S. et al. (2020). The seismicity
459 of Mars. Nature Geosciences 13: 205 – 212.
460 Goetz, W., Pike, W. T., Hviid, S. F., Madsen, M. B., Morris, R. V., Hecht, M. H. et al., (2010). Microscopy
461 analysis of soils at the Phoenix landing site, Mars: Classification of soil particles and description of
462 their optical and magnetic properties. Journal of Geophysical Research E: Planets, 115(8), 1–23.
463 https://doi.org/10.1029/2009JE003437
464 Golombek, M., Kipp D., Warner I.J., Daubar I.J., Fergason R.L., Kirk R.L. et al. (2017). Selection of the
465 InSight landing site. Space Science Review 211, 5–95.
466 Golombek M, Warner NH, Grant JA, Hauber E, Ansan V, Weitz CM et al (2020). Geology of the InSight
467 landing site on Mars. Nat Commun 11(1):1014. https://doi.org/10.1038/s41467-020-14679-1
468 Golombek M., T. Hudson, P. Bailey, N. Balabanska, E. Marteau, C. Charalambous et al. (2023). Results
469 from InSight Robotic Arm Activities. Space Science Review, 219:20 doi:10.1007/s11214-023-00964-
470 0
471 Grott M., T. Spohn, J. Knollenberg, C. Krause, T.L. Hudson, S. Piqueux et al., (2021). Thermal
472 Conductivity of the Martian Soil at the InSight Landing site from HP3 Active Heating Experiments.
473 Journal of Geophysical Research - Planets, doi 10.1002/essoar.10506340.1.
474 Hariprasad, C., Rajashekhar, M. & Umashankar, B. Preparation of Uniform Sand Specimens Using
475 Stationary Pluviation and Vibratory Methods (2016). Geotechnical and Geological Engineering 34,
476 1909–1922. https://doi.org/10.1007/s10706-016-0064-0
477 Haskin, L. A. et al. Water alteration of rocks and soils from the Spirit rover site, Gusev crater, Mars. Nature
478 436, 66–69 (2005).
479 Henkel, D. J. and Gilbert, G. D. (1952). The effect measured of the rubber membrane on the triaxial
480 compression strength of clay samples. Géotechnique, 3(1), 20–29.
481 Hobiger, M., Hallo, M., Schmelzbach, C., Stähler, S. C., Fäh, D., Giardini, D. et al. (2021). The shallow
482 structure of Mars at the InSight landing site from inversion of ambient vibrations. Nature
483 communications, 12(1), 1-13.
484 Hurowitz, J. A. et al. In situ and experimental evidence for acidic weathering of rocks and soils on Mars. J.
485 Geophys. Res. 111, E02S19 (2006).

Jamiolkowski, M., Lancellotta, R. and Lo Presti D.C.F. (1995). Remarks on the stiffness at small strains of six Italian clays. Proc. Symposium on Pre-failure Deformation Behaviour of Geomaterials, 817 – 836, Balkema. https://www.researchgate.net/publication/306157192

Jovičić, V., Coop, M. and. Simic. M. (1996): Objective criteria for determining Gmax from bender element tests, Géotechnique, 46(2), 357-362.

Kolbuszewski J.J. (1948). An empirical study of maximum and minimum porosities of sand. In: Proceedings of Second International Conference on Soil Mechanics and Foundation Engineering, Rotterdam, Netherland: ISSMGE, vol 1, pp 158–165

Kumar, J. and Madhusudhan, B. N. (2010). Effect of relative density and confining pressure on Poisson ratio from bender and extender elements tests. Géotechnique, 60(7), 561-567.

Lee, J.-S. and Santamarina, J. C. (2005). Bender Elements: Performance and Signal Interpretation. Journal of geotechnical and geoenvironmental engineering. 131(9), 1063-1070. https://doi.org/10.1061/ASCE1090-02412005131:91063

Lognonné, P., Banerdt, W. B., Giardini, D., Pike, W. T., Christensen, U., Laudet, P. et al. (2019). SEIS: Insight's seismic experiment for internal structure of Mars. Space Science Reviews, 215(1), 1-170.

Lognonné P., Banerdt W. B., Pike W. T., Giardini D., Christensen U., Garcia R. F. et al., (2020). Constraints on the shallow elastic and anelastic structure of Mars from InSight seismic data. Nature Geoscience, https://doi.org/10.1038/s41561-020-0536-y.

Marteau E, Golombek M, Vrettos C, Garvin JB, Williams NR (2021). Soil mechanical properties at the InSight landing site, Mars. In: 52nd Lunar and Planetary Science Conference, abstract #2067, Houston.

Marteau E, Golombek M, Vrettos C, Delage P, Williams NR, Ansan V (2022). Soil strength properties derived from scraping and dumping activities at the InSight landing site on Mars. In: 53rd Lunar and Planetary Science Conference. Abstract #1523, Houston.

Marteau E, Golombek M, Delage P, Vrettos C, Hurst K, Gomez A et al. (2023). Initial results from the Insight lander robotic arm soil mechanics experiments on Mars. 54th Lunar and Planetary Science Conference. Abstract #1597, Houston.

Morgan, P., Grott, M., Knapmeyer-Endrun, B., Golombek, M., Delage, P., Lognonné, P. et al. (2018). A pre-landing assessment of regolith properties at the InSight landing site. Space Science Reviews, 214(6), 1-47.

Mohsin, A. K. M. and Airey D. W. (2003): Automating Gmax measurement in triaxial test. Deformation characteristics of Geomaterials, Proceedings 3rd International Symposium IS Lyon. Balkema, Lyon, 73-80.

Murillo, C. A., Thorel, L. and Caicedo, B. (2009). Spectral analysis of surface waves method to assess shear wave velocity within centrifuge models. Journal of Applied Geophysics, 68(2), 135–145. https://doi.org/10.1016/j.jappgeo.2008.10.007

Murillo, C., Sharifipour, M., Caicedo, B., Thorel, L. and Dano, C. (2011). Elastic parameters of intermediate soils based on bender-extender elements pulse tests. Soils and Foundations, 51(4), 637-649.

Nakagawa, K., Soga, K. & Mitchell, J. K. (1996). Pulse transmission system for measuring wave propagation in soils. J. Geotech. Engng Div., ASCE 122(4), 302–308.

Newland, P. L. and Allely, B. H. (1959). Volume changes during undrained triaxial tests on saturated dilatant granular materials. Géotechnique, 9(4), 174–182.

Prasad, M. (2002). Acoustic measurements in unconsolidated sands at low effective pressure and overpressure detection. Geophysics, 67(2), 405–412. https://doi.org/10.1190/1.1468600

Posiolova, L. V., Lognonné, P., Banerdt, W. B., Clinton, J., Collins, G. S., Kawamura, T. et al. (2022). Largest recent impact craters on Mars: Orbital imaging and surface seismic co-investigation. Science, 378(6618), 412-417.

Seiferlin K., Ehrenfreund P., Garry J., Gunderson K., Hütter E., Karg G. et al. (2008). Simulating Martian regolith in the laboratory. Planetary and Space Science 56: 2009 – 2025

Shirley, D. J. and Hampton, L. D. (1978). Shear-wave measurements in laboratory sediments. The Journal of the Acoustical Society of America, 63(2), 607-613. http://acousticalsociety.org/content/terms.

Spohn, T., Grott, M., Smrekar, S. E., Knollenberg, J., Hudson, T. L., Krause, C. et al. (2018). The Heat Flow and Physical Properties Package (HP3) for the InSight Mission. In Space Science Reviews (Vol. 214, Issue 5). The Author(s). https://doi.org/10.1007/s11214-018-0531-4

Spohn, T., Hudson, T. L., Marteau, E., Golombek, M., Grott, M., Wippermann, T. et al. (2022a). The InSight HP3 Penetrator (Mole) on Mars: Soil Properties Derived From the Penetration Attempts and Related Activities. Space Science Reviews (2022) 218:72, https://doi.org/10.1007/s11214-022-00941-z

Spohn, T., Hudson, T. L., Witte, L., Wippermann, T., Wisniewski, L., Kedziora, B. et al. (2022b). The InSight-HP^3 mole on Mars: Lessons learned from attempts to penetrate to depth in the Martian soil. Advances in Space Research, 69(8), 3140-3163, doi :10.1007/s11214-022-00941-z.

Suwal, L. P. and Kuwano, R. (2013). Statically and dynamically measured Poisson's ratio of granular soils on triaxial laboratory specimens. Geotechnical Testing Journal, 36(4), 493-505.

Verdier N., Ansan V., Delage P., Ali K.S., Beucler E., Charalambous C. et al. (2023). Using wind dispersion effects during the InSight tether burial activities to better constrain the regolith grain size distribution. Revised version submitted, Journal of Geophysical Research – Planets.

552 Viggiani, G. and Atkinson, J. H. (1995a). Stiffness of fine-grained soil at very small strains. Géotechnique,
553 45(2), 249–265.
554 Viggiani, G. and Atkinson, J. H. (1995b). Interpretation of bender element tests. Géotechnique, 45(1), 149–
555 154.
556 Vilhar, G. & Jovičić, V., (2009). Measurement And Interpretation Of The Small Strain Stiffness Of Boštanj
557 Silty San. Acta Geotechnica Slovenica. 6(2), 57-75
558 Wang, Y., Benahmed, N., Cui, Y. J. and Tang, A. M. (2017). A novel method for determining the small-
559 strain shear modulus of soil using the bender elements technique. Canadian Geotechnical Journal,
560 54(2), 280–289. https://doi.org/10.1139/cgj-2016-0341
561 Warner N. H., M. P. Golombek , V. Ansan, E. Marteau , N. Williams , J. A. Grant et al. (2022). In Situ and
562 Orbital Stratigraphic Characterization of the InSight Landing Site—A Type Example of a Regolith-
563 Covered Lava Plain on Mars. Journal of Geophysical Research – Planets, doi 10.1029/2022JE007232
564 Zimmer, M., Prasad, M., & Mavko, G. (2002). Pressure and porosity influences on V_P-V_S ratio in unconsolidated
565 sands. The Leading Edge, 21(2):178-183, https://doi.org/10.1190/1.1452609.
566

567 **Open Research**

568 All the Waveform data csv files from the Bender Element measurements performed on the four
569 samples, used for wave velocity calculations in the study are available at the public MRA-
570 Bender-element-repository repository (Castillo-Betancourt Juan Pablo. (2023)). Instructions may
571 be found on the “README” file of the repository.
572
573

Appendix A: Methodology for travel time determination

A Matlab script was developed to enable accurate and quick identification of the departing and arrival times on a considerable amount of data within a reasonable timeframe (about 150 waves were acquired in each of the four experimental programs, with a total of 1200 wave measures to analyse).

The MATLAB script allows to simultaneously consider up to three methodologies for identifying the departing and arrival times. The procedure identifies local maximum, minimum and zero values, that make up the potential points of interest of the signal (shown in Figure A1). This identification is an automatic initialisation method of suggested arrival and departure points. To achieve this, the following procedure was implemented.

1. Initially, a set of candidates for local maximums and minimums is established after evaluating the sign function of numerically calculated derivatives between every point in the signal and its surrounding neighbours. This procedure is a recursive method based on a parameter selected to determine an adequate number of points (seeking to not saturate the visual interface with too many choices of potential candidate points).
2. After that, the search is widened from each candidate point by following the curve up to the previous existing inflection point (or the beginning of the signal, should it be the case). A new candidate point is then proposed.

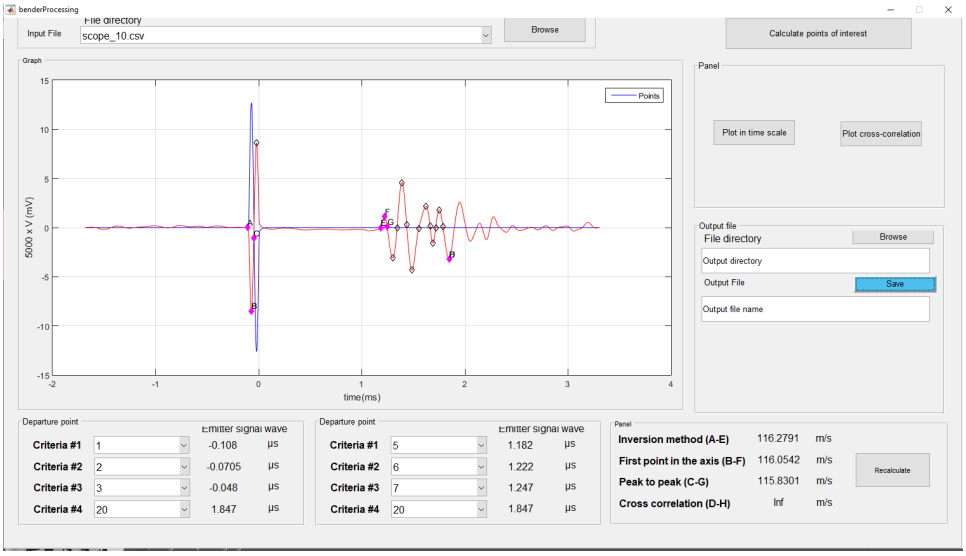

Figure A1. The interface of the Matlab script for single wave data analysis.

The script also allows simultaneous visualisation of the waves under various confining stresses, as seen in Figure A2. All the signals acquired at the same stress value are averaged to account for variability and repeatability. By observing all the measures, the user can choose the time arrival points by clicking on a visual interface.

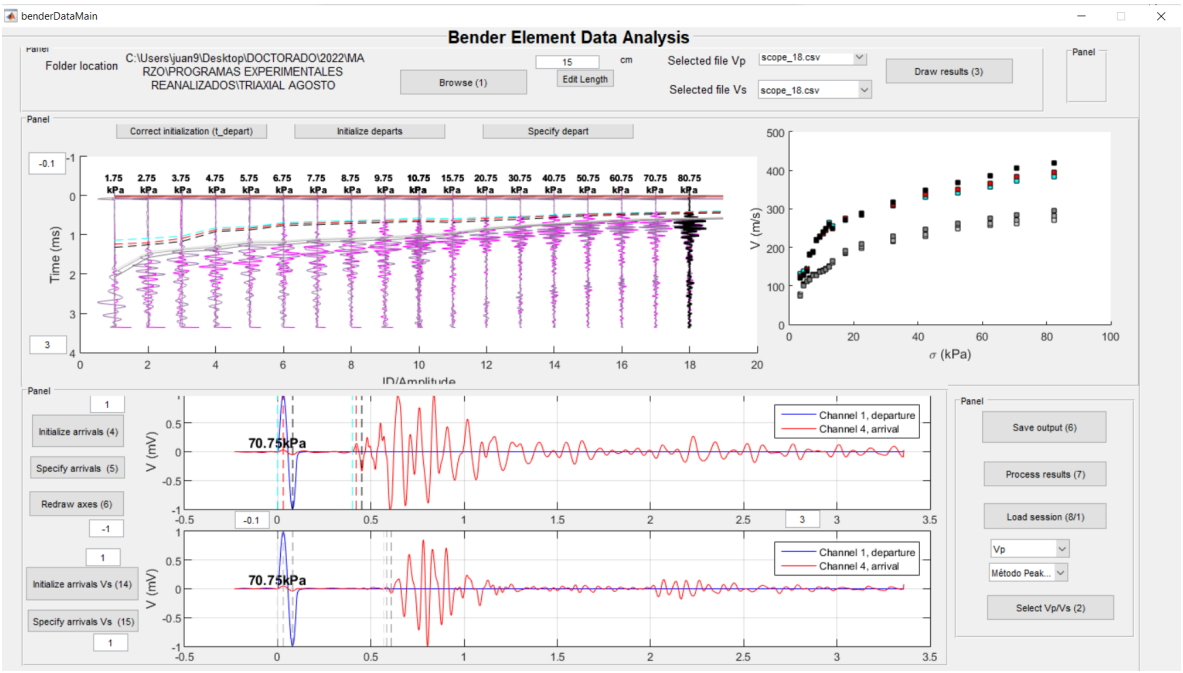

Figure A2. Interpretation script showing all waves measured at different stresses.

Proper signal visualisation is critical when using Wang's arrival time approach, because it requires viewing P and S waves simultaneously on the same timescale, as seen in Figure A2. In contrast to usual methods like peak-to-peak or arrival-to-arrival, a matching of P and S wave signals are compared . While determining the P wave arrival time is relatively simple (the choice is given by the first departure of the signal from the zero axis in the P signal), Wang's criterion indicates that the location of the S wave arrival time correspond to the peak of the "initial main excursion in the opposite direction of movement compared to that of the S-wave received signal". This means that the first sizeable negative peak in S wave will characterise the S wave arrival time. Choosing this last peak can often be a challenge and the associated P wave hence allows an objective and repeatable measurement. The chosen point for the S wave arrival time is to be found at the exact location when the first negative peak with considerable amplitude appears in the P wave signal, indicating the arrival of the S components produced by this P wave signal. This also implies that the motion registered in the S wave signal before the chosen time of arrival corresponds to the

615 faster P wave produced by the action of the bender that emitted the S wave and its rebounds on the
616 sample walls.
617 Figure A3 shows an example of the waveforms acquired during one of the four experimental
618 programs, along with lines marking the identified locations of the departure and arrival of the
619 waves for the three utilised criteria.

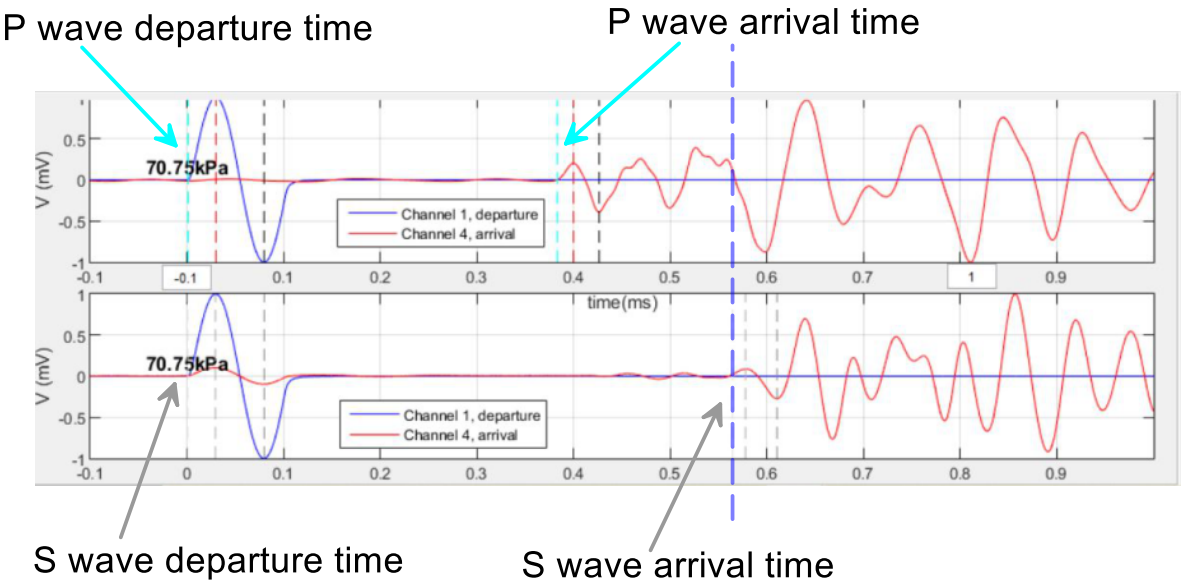

620

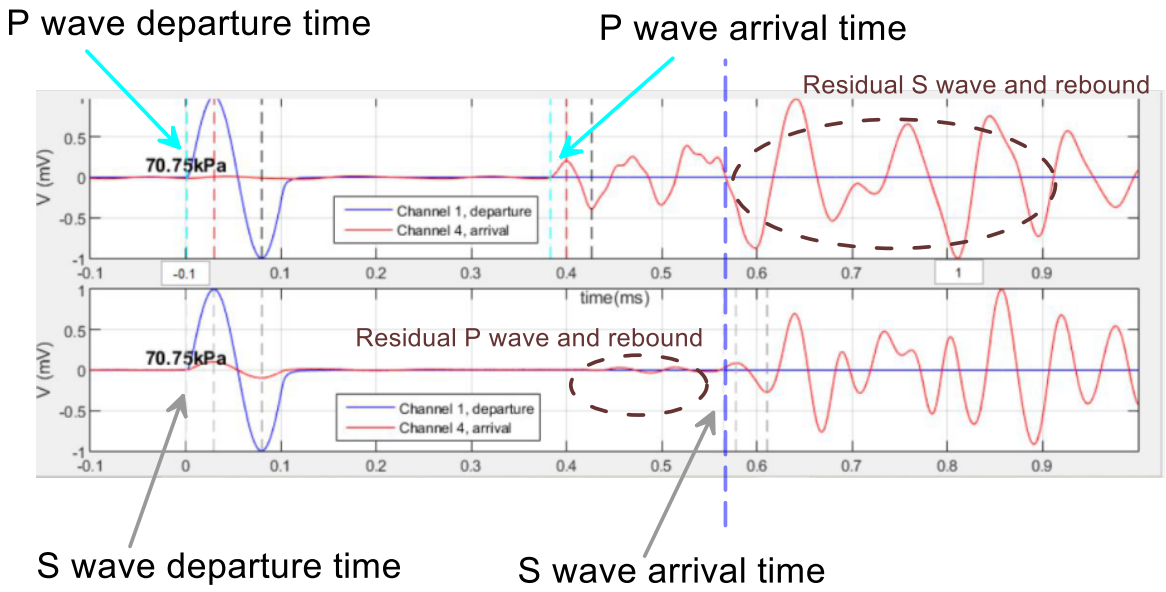

621

622 **Figure A3**. Simultaneous visualisation of the P and S waves following Wang's method.

623

The following figures present the waves acquired during the other three experimental programs, along with the lines identifying the departure and arrival times for both P and S waves. The figures are shown as generated in the data processing tool built for data interpretation.

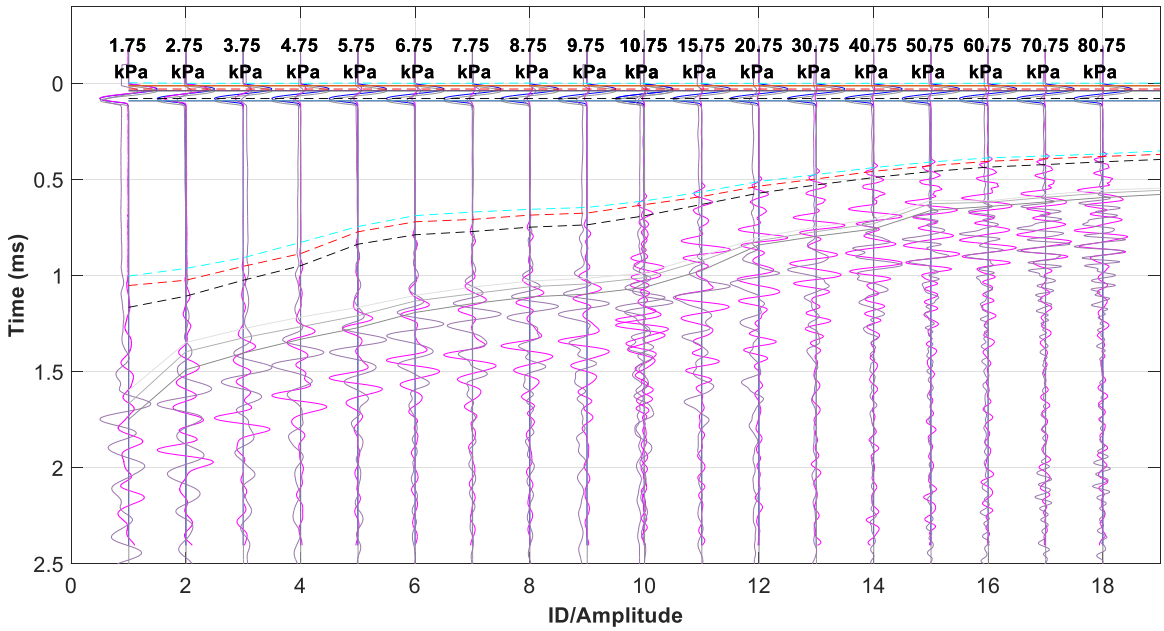

Figure A4. Waves acquired on sample EP1. Depart and arrival times are indicated both for P and S waves.

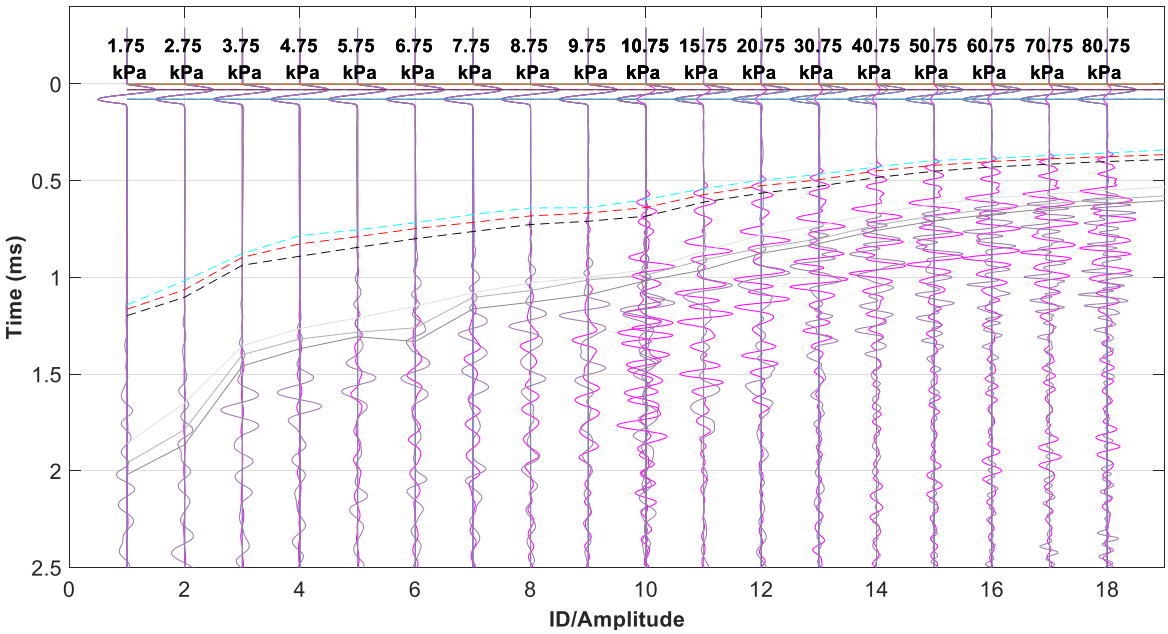

Figure A5. Waves acquired on sample EP2. Depart and arrival times are indicated both for P and S waves.

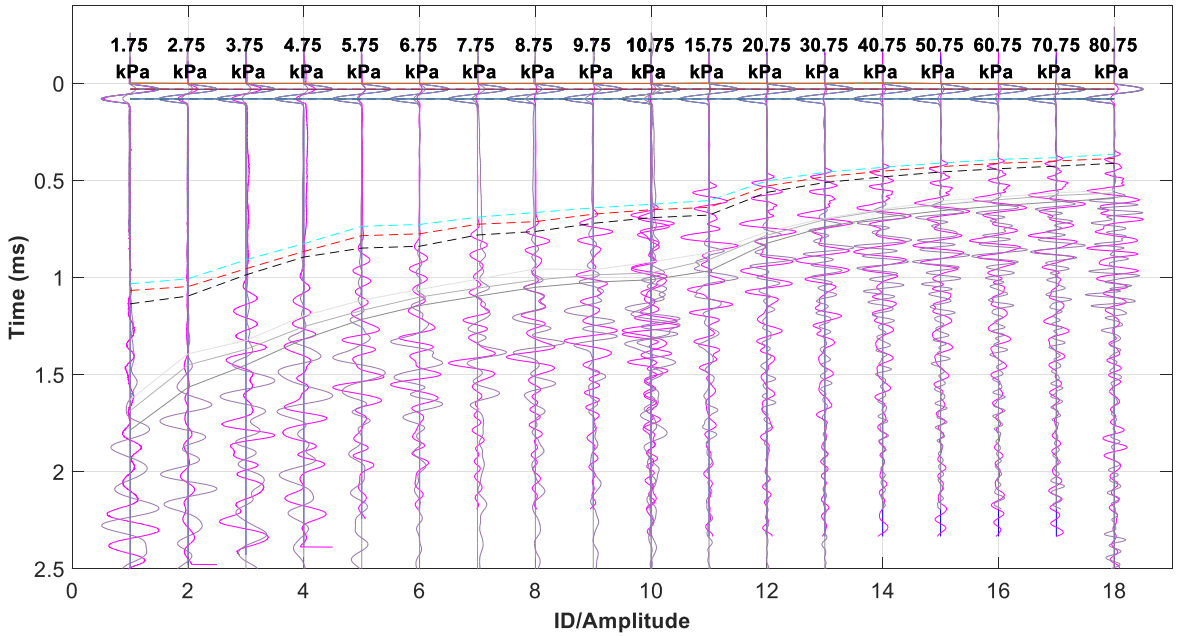

Figure A6. Waves acquired on sample EP3. Depart and arrival times are indicated both for P and S waves.

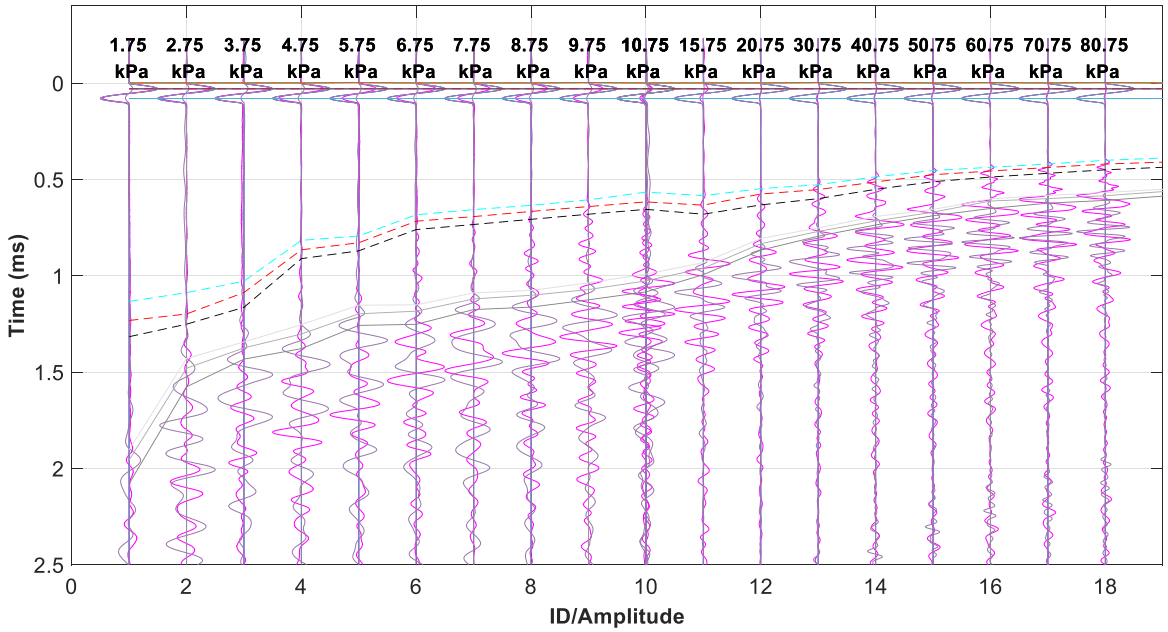

Figure A7. Waves acquired during on sample EP4. Depart and arrival times are indicated both for P and S waves.